ADVANCED ENERGY MATERIALS
www.advenergymat.de

Check for updates

Copper–Nickel Nitride Nanosheets as Efficient Bifunctional Catalysts for Hydrazine-Assisted Electrolytic Hydrogen Production

Zhaoyang Wang, Lin Xu, Fuzhi Huang, Longbing Qu, Jiantao Li, Kwadwo Asare Owusu, Ziang Liu, Zifeng Lin, Binhua Xiang, Xiong Liu, Kangning Zhao, Xiaobin Liao, Wei Yang, Yi-Bing Cheng, and Liqiang Mai**

Electrocatalytic water splitting is one of the sustainable and promising strategies to generate hydrogen fuel but still remains a great challenge because of the sluggish anodic oxygen evolution reaction (OER). A very effective approach to dramatically decrease the input cell voltage of water electrolysis is to replace the anodic OER with hydrazine oxidation reaction (HzOR) due to its lower thermodynamic oxidation potential. Therefore, developing the low-cost and efficient HzOR catalysts, coupled with the cathodic hydrogen evolution reaction (HER), is tremendously important for energy-saving electrolytic hydrogen production. Herein, a new-type of copper–nickel nitride (Cu_1Ni_2-N) with rich Cu_4N/Ni_3N interface is rationally constructed on carbon fiber cloth. The 3D electrode exhibits extraordinary HER performance with an overpotential of 71.4 mV at 10 mA cm^{-2} in 1.0 M KOH, simultaneously delivering an ultralow potential of 0.5 mV at 10 mA cm^{-2} for HzOR in a 1.0 M KOH/0.5 M hydrazine electrolyte. Moreover, the electrolytic cell utilizing the synthesized Cu_1Ni_2-N electrode as both the cathode and anode display a cell voltage of 0.24 V at 10 mA cm^{-2} with an excellent stability over 75 h. The present work develops the promising copper–nickel-based nitride as a bifunctional electrocatalyst through hydrazine-assistance for energy-saving electrolytic hydrogen production.

1. Introduction

With the fast fossil fuel exhaustion and associated increasingly serious environmental pollution, it is very urgent to explore green and renewable energy resources in order to deal with this situation.[1,2] Hydrogen with high energy density has been regarded as an ideal alternative energy carrier due to its purity and sustainability.[3,4] Production of hydrogen by electrochemical water splitting in alkaline electrolyte which involves two half reactions, namely, the hydrogen evolution reaction (HER, $4H_2O + 4e^- \rightarrow 2H_2 + 4OH^-$) and oxygen evolution reaction (OER, $4OH^- \rightarrow O_2 + 2H_2O + 4e^-$), seems a promising and environmentally benign approach.[5–7] At present, precious metal electrocatalysts, such as platinum-based and iridium or ruthenium-based materials are regarded as the state-of-the-art catalysts for HER and OER, respectively.[8–10] However, the high cost, low abundance, and poor stability of these catalysts significantly hinder their extensive applications in commercial electrolyzers. Consequently, extensive studies have been conducted to develop low-cost, high-activity electrocatalysts based on transitional metal materials, including metal alloys,[11,12] chalcogenides,[13–17] phosphides,[18–22] carbides,[23–25] and nitrides[26–31] for HER, and metal oxides,[32,33] hydroxides,[34] oxyhydroxides,[35,36] selenides,[37–41] and perovskites[42] for OER. Nevertheless, the operation voltage of water splitting in alkaline electrolyte at 10 mA cm^{-2} is still larger than 1.4 V because of the sluggish anodic OER kinetics.[18–20,34] OER is quite a complicated process as it involves four proton-coupled electrons transfer steps, O—H bond breaking and O—O bond

Z. Y. Wang, Prof. L. Xu, Prof. F. Z. Huang, Dr. J. T. Li, K. A. Owusu, Z. A. Liu, Z. F. Lin, B. H. Xiang, X. Liu, Dr. K. N. Zhao, W. Yang, Prof. Y.-B. Cheng, Prof. L. Q. Mai
State Key Laboratory of Advanced Technology for Materials Synthesis and Processing
Wuhan University of Technology
Hubei, Wuhan 430070, P. R. China
E-mail: fuzhi.huang@whut.edu.cn; mlq518@whut.edu.cn

The ORCID identification number(s) for the author(s) of this article can be found under https://doi.org/10.1002/aenm.201900390.

DOI: 10.1002/aenm.201900390

L. B. Qu
Department of Mechanical Engineering
University of Melbourne
Parkville, VIC 3010, Australia

X. B. Liao
State Key Laboratory of Silicate Materials for Architectures
Wuhan University of Technology
Wuhan 430070, P. R. China

Prof. Y.-B. Cheng
ARC Centre of Excellence in Exciton Science
Monash University
Clayton, VIC 3800, Australia

 © 2019 WILEY-VCH Verlag GmbH & Co. KGaA, Weinheim

formation.[43] Accordingly, OER has been recognized as the main limitation in the development of water electrolyzers.

Recent researches have shown a promising strategy to overcome this bottleneck by replacing OER with electrochemical oxidation of more favorably oxidized molecules, such as methanol,[44] ethanol,[45] glycol,[46] benzyl alcohol,[27] urea,[46–51] 5-hydroxymethylfurfural[52] and hydrazine.[53–55] These molecules could be readily oxidized and converted into other chemicals at lower thermodynamic potentials than that of OER (1.23 V vs reversible hydrogen electrode, RHE) at the anode, thus remarkably decreasing the cell voltage for hydrogen production. Yu et. al synthesized highly porous $NiMoO_4$ nanorods by annealing treatment in Argon atmosphere, which exhibits an extraordinary catalytic activity for urea oxidation reaction (UOR, $CO(NH_2)_2 + 6OH^- \rightarrow N_2 + CO_2 + 5H_2O + 6e^-$, 0.37 V vs RHE).[48] The anodic electrode requires just a low potential of 1.37 V vs RHE at 10 mA cm^{-2} in 1 M KOH/0.5 M urea electrolyte. Meanwhile, the urea electrolyzer delivers a small cell voltage of 1.38 V at 10 mA cm^{-2}. Compared with UOR, hydrazine oxidation reaction (HzOR, $N_2H_4 + 4OH^- \rightarrow N_2 + 4H_2O + 4e^-$, –0.33 V vs RHE) possesses an even lower standard potential.[53,55] Moreover, this anodic oxidation process only produces nitrogen and water, without any greenhouse gases emission. These advantages indicate that HzOR has a great potential to replace OER for water electrolysis. Accordingly, developing the bifunctional catalysts with high electrocatalytic activity toward both anodic HzOR and cathodic HER is an effective strategy for hydrogen production. As known, a bifunctional catalyst can not only avoid the side reactions induced by different catalysts, but also greatly simplify the catalytic electrode design and construction.[56,57] Recently, great attention has been paid to exploring high performance catalysts for HzOR, including noble metal (Pt, Pd),[58,59] non-noble metal and alloys (Ni, Co, NiCo, NiZn),[55,60,61] chalcogenides (NiS_2, CoS_2, $CoSe_2$),[53,54,62] and phosphides (Ni_2P, FeP, Cu_3P).[63–65] However, fabricating the bifunctional catalytic electrode with superior HER and HzOR activities toward hydrazine-assisted energy-saving hydrogen production is still a tremendous challenge, needing innovative development of high-performance catalysts. Preparing the bimetal-based catalysts with novel components and architectures by interfacial engineering is a practicable strategy to improve this situation.[14,66–69] The interfacial modification approach will expose more active sites, optimize the electronic environment, adjust the catalytic reaction intermediates adsorption, and favor the electron and mass transportation. Both theoretical calculations and experimental explorations have indicated that the electrocatalytic performance of bimetal catalysts can be more easily optimized than that of the corresponding individual compounds.[26,27,29,70–72] Chai and co-workers reported a series of promising bimetal catalysts, such as $Ni_{0.6}Co_{1.4}P$,[70] Ni-Fe-P,[71] and $Fe_{0.125}Ni_{0.875}Se_2$,[72] which have been demonstrated for efficient water electrolysis. Lin and co-workers developed a bimetallic copper-cobalt-based phosphide with nitrogen-doped carbon ($Cu_{0.3}Co_{2.7}P$/NC) as a bifunctional electrocatalyst in alkaline solution.[21] Cu incorporation could effectively modify the electronic structure and optimize the intermediate adsorption energy to accelerate the catalytic kinetics. The synergetic effects between two different host atoms or components endow the compound with an outstanding catalytic potential. Considering the good metallic conductivity, low electrical resistance, and superior corrosion stability, metal nitrides have been paid extensive attention for water electrolysis.[26,27,29–31] To the best of our knowledge, copper–nickel-based nitride used as a bifunctional electrocatalyst for HER and HzOR has been rarely reported. Based on these concerns, it could be hypothesized that constructing the bimetallic copper–nickel-based nitride with nickel nitride/copper nitride interface might provide a new approach to achieving exceptional bifunctional electrocatalyst through hydrazine-assistance for energy-saving electrolytic hydrogen production.

Herein, we constructed copper–nickel nitride (Cu_1Ni_2-N) porous nanosheets supported on carbon fiber cloth (CFC), which was prepared using copper–nickel layered double hydroxide (CuNi-LDH) precursor through a thermal ammonolysis process. The 3D catalyst electrode exhibits outstanding performance for both HER and HzOR. Specifically, Cu_1Ni_2-N electrode shows an overpotential of 71.4 mV at 10 mA cm^{-2} in 1 M KOH, simultaneously delivering an ultralow potential of 0.5 mV at 10 mA cm^{-2} for HzOR in 1.0 M KOH/0.5 M hydrazine electrolyte. Furthermore, when the bifunctional catalyst electrode was utilized as cathode and anode, a water electrolysis system is operated at a cell voltage of a mere 0.24 V to reach the current density of 10 mA cm^{-2} with 75 h durability in the alkaline electrolyte with hydrazine. The exceptional performance can be ascribed to the high electrical conductivity, porous morphology of interconnected nanostructures with large surface area, superhydrophilic electrode surface, and synergistic catalytic effects of nickel nitride and copper nitride. Moreover, the hydroxide species, disordered structures, and rich defects generated during the catalytic reactions might also contribute to promoting the catalytic activity.

2. Results and Discussion

As schematically illustrated in **Figure 1**, Cu_1Ni_2-N nanosheets supported on CFC were prepared through a two-step process and the synthesis details have been described in Supporting Information. First, the Cu_1Ni_2-LDH nanosheet precursor was synthesized by a facile solvothermal treatment of $Cu(NO)_2 \cdot 3H_2O$, $Ni(NO)_2 \cdot 6H_2O$ and hexamethylene tetramine (HMT) in methanol at 180 °C for 12 h.[73] A subsequent thermal ammonolysis process at 400 °C for 2 h was undertaken to obtain the Cu_1Ni_2-N electrode. Figure S1A, Supporting Information, presents the X-ray diffraction (XRD) spectrum of Cu_1Ni_2-based precursor, which exhibits a typical layered structure. The diffraction peaks observed at 10.9°, 21.8°, and 33.6° can be assigned to the (003), (006), and (009) planes of hydrotalcite, respectively.[74] As shown in the scanning electron microscopy (SEM) images of Figure S1B,C, Supporting Information, the Cu_1Ni_2-LDH precursor nanosheets with smooth surface are uniformly wrapped on the CFC. These nanosheets with a thickness of 20–30 nm are in close contact forming a network. Energy-dispersive X-ray (EDX) spectrum displays the existence of Cu and Ni with an atomic ratio of 1:2.4. Similarly, $Ni(OH)_2 \cdot xH_2O$ is confirmed as the Ni-based precursor, which also appears as a layered structure with nanosheet networks morphology (Figure S1D–F, Supporting Information). Cu-based

© 2019 WILEY-VCH Verlag GmbH & Co. KGaA, Weinheim

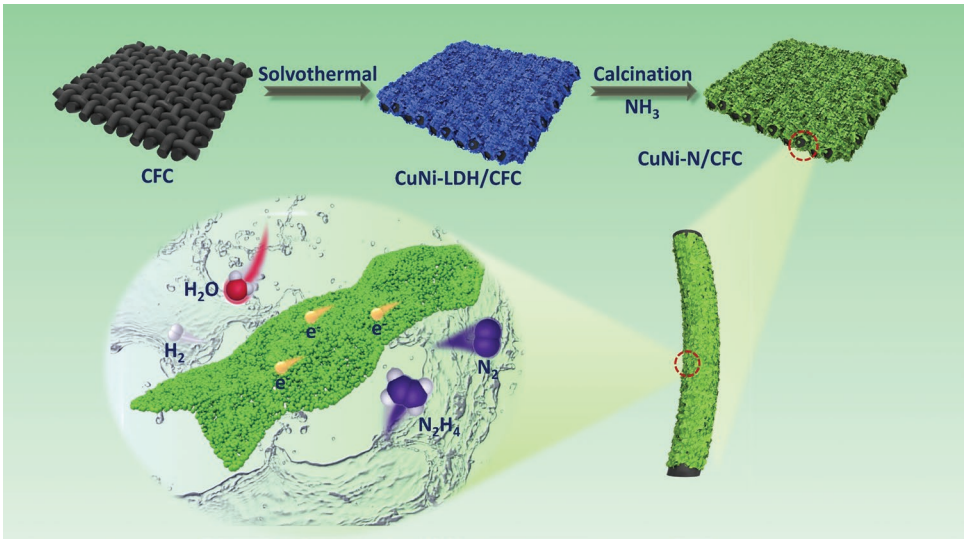

Figure 1. Schematic illustration of the formation process of Cu_1Ni_2-N/CFC electrode.

precursor was synthesized through a typical hydrothermal method, which could be attributed to $Cu_2CO_3(OH)_2$ phase with nanobelt morphology from the XRD pattern and SEM images (Figure S4, Supporting Information). After thermal ammonolysis treatment, the hydroxide or subcarbonate precursors were converted into metal nitrides. XRD spectrum of the prepared Cu_1Ni_2-N electrode is shown in **Figure 2**A. Compared with CFC, for the pattern of Cu_1Ni_2-N, the peaks located at 38.5°, 42.3°, 44.3°, and 70.8° can be assigned to the (110), (002), (111), and (300) planes of Ni_3N, respectively (JCPDS No. 10–0280) and the peaks at 41.3° and 47.9° match well with the (111) and (200) planes of Cu_4N, respectively (JCPDS No. 47–1072). As

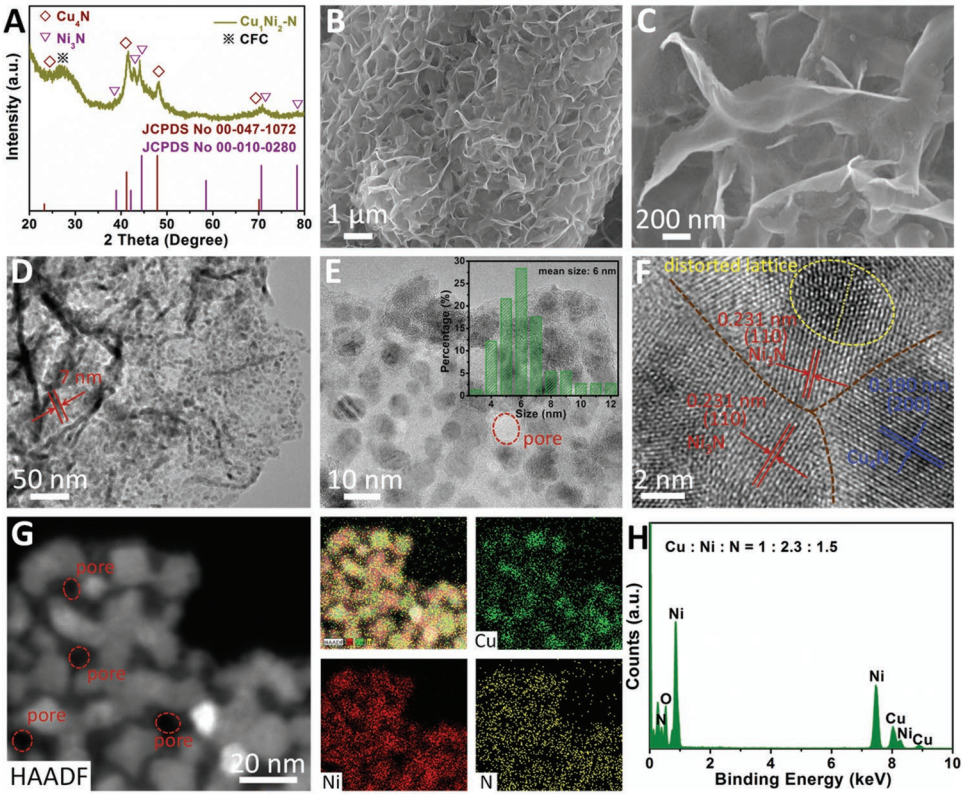

Figure 2. A) XRD pattern for Cu_1Ni_2-N/CFC. B) Low-magnification and C) high-magnification SEM images of typical morphology for Cu_1Ni_2-N/CFC. D,E) TEM (inset shows the particle size distribution) and F) HRTEM images of Cu_1Ni_2-N/CFC. G) HAADF-STEM image and corresponding elemental mapping. H) The corresponding EDX spectrum.

© 2019 WILEY-VCH Verlag GmbH & Co. KGaA, Weinheim

shown in the SEM images (Figure S2A,B, Supporting Information; Figure 2B,C), the nanosheets morphology of Cu_1Ni_2-LDH can be well reserved after annealing in NH_3. Moreover, Cu_1Ni_2-N nanosheets become rough and thinner with a thickness of ≈7 nm and a lateral length of ≈1.5 µm, which form networks supported on the CFC with a large coverage. Such highly open and interconnected network could promote the accessibility of electrolyte and accelerate the electron transport. The transmission electron microscopy (TEM) images are shown in Figure 2D,E, which verify that the surface of the nanosheet are composed of several nanoparticles with an average size of 6 nm. In comparison, the nanoparticles on the surface of Ni_3N nanosheets are bigger in dimensions with an average size of 21 nm (Figure S3D, Supporting Information). In the high-resolution transmission electron microscopy (HRTEM) image of Cu_1Ni_2-N (Figure 2F), the overlapping lattice fringe with an interplanar spacing of 0.231 nm can be indexed to the (110) crystal planes of Ni_3N and the interplanar distance of 0.190 nm can be indexed to the (200) planes of Cu_4N. Notably, the distorted lattice structure can be observed (labeled by the yellow oval), which is derived by the mismatch of the two kinds of nitrides. The distorted lattice arrangement may offer additional active sites for catalytic reactions.[40] In addition, the high angle annular dark field scanning TEM (HAADF-STEM) and element mapping analysis reveal that the Cu, Ni, and N elements are distributed on the whole Cu_1Ni_2-N nanosheet. The corresponding EDX spectrum confirms that the atomic ratio of Cu to Ni is 1:2.3. We compared the electrical conductivity of Cu_1Ni_2-N and Ni-N based on the *I–V* curves (Figure S5, Supporting Information). The conductivity of Cu_1Ni_2-N is 8.1×10^3 S m^{-1}, much higher than that of Ni-N (5.4×10^3 S m^{-1}). Note that the electric conductivity of copper–nickel nitride is superior to that of nickel nitride, which is similar with the previous results of bimetallic catalysts.[18,41] The improved conductivity can be attributed to the enhanced carrier density near the Fermi level induced by the strong coupling interactions between nickel nitride and copper nitride.[26,28] The surface area and pore size of the Cu_1Ni_2-N nanosheets are determined by N_2 sorption measurements. As shown in Figure S6, Supporting Information, the Brunauer–Emmett–Teller (BET) specific surface area is 61.83 m^2 g^{-1} for Cu_1Ni_2-N, which is about two times higher than that of Ni-N (32.39 m^2 g^{-1}). Although Cu_1Ni_2-N and Ni-N exhibit similar pore-size distribution (0–50 nm), Cu_1Ni_2-N displays a much higher pore volume of 0.2 cm^3 g^{-1} than that of Ni-N (0.05 cm^3 g^{-1}). The porous structure and large surface area could provide more active sites, enable more contact area with the electrolyte, and contribute toward fast mass transport, which are considered to be beneficial for electrocatalysis.[18,27,41] The contact angle was measured to reveal the accessibility of electrolyte into the Cu_1Ni_2-N electrode. Comparatively, the bare CFC displays a superhydrophobic nature with a contact angle of 143° while the Cu_1Ni_2-N electrode presents superhydrophilic behavior with a very small contact angle of nearly 0° (Figure S7 and Movie S1, Supporting Information). This result implies that the improved electrolyte wettability ensures the sufficient contact, promoting electrocatalytic reactions.

The surface chemical composition and elemental valence state of the as-prepared Cu_1Ni_2-N and Ni-N were acquired through the X-ray photoelectron spectroscopy (XPS) analysis. As shown in Figure S8, Supporting Information, the survey spectrum of Cu_1Ni_2-N reveals the presence of Cu, Ni, and N elements, which is consistent with the elemental mapping results. The high-resolution spectrum of Cu 2p can be deconvoluted into four peaks as shown in **Figure 3**A. The peaks located at 932.3 and 952.1 eV are ascribed to Cu $2p_{3/2}$ and Cu $2p_{1/2}$, respectively, corresponding to Cu^0/Cu^+ state. Meanwhile, the peaks at 942.7 and 961.9 eV can be attributed to satellite peaks of Cu. The binding energy centered at 934.6 and 954.7 eV are assigned to Cu^{2+} species. In Figure 3B, the Ni 2p spectrum of Cu_1Ni_2-N exhibits two main peaks of Ni $2p_{3/2}$ at 852.6 and 855.2 eV with a satellite peak at 861.4 eV, which are related to Ni^0 and Ni^{2+} and the satellite peak. The Ni^0 state indicates a metallic feature of Cu_1Ni_2-N, which is consistent with previous reports.[26,28] Compared to the Ni $2p_{3/2}$ region of Ni-N, the binding energy exhibits a negative shift of about 0.5 eV. The N 1s spectrum of Cu_1Ni_2-N can be deconvoluted into two peaks. The peak located at 398.5 eV is assigned to N—Ni/Cu bonds, which further confirms the formation of the nitride. Another peak at 399.2 eV is ascribed to N—H bonds, which indicates the presence of a number of H species on the catalyst surface. Similarly, in comparison with N 1s spectrum of Ni-N, the binding energy of N–metal displays a negative shift of about 0.3 eV. XPS results suggest the existence of strong electronic interactions between Ni_3N and Cu_4N, which may induce the redistribution of charge on the coupling interfaces.[15,49,75,76]

To evaluate the electrocatalytic performance for HER, Cu_1Ni_2-N electrode was tested in 1.0 M KOH solution using a typical three-electrode configuration. For comparison, bare CFC, Ni-N, Cu-N, Cu_1Ni_2-LDH, $Ni(OH)_2$, Cu-pre, commercial Pt/C, and IrO_2 supported on CFC were also evaluated as control experiments. The linear sweep voltammetry (LSV) curves of the different samples were corrected for iR compensation. As shown

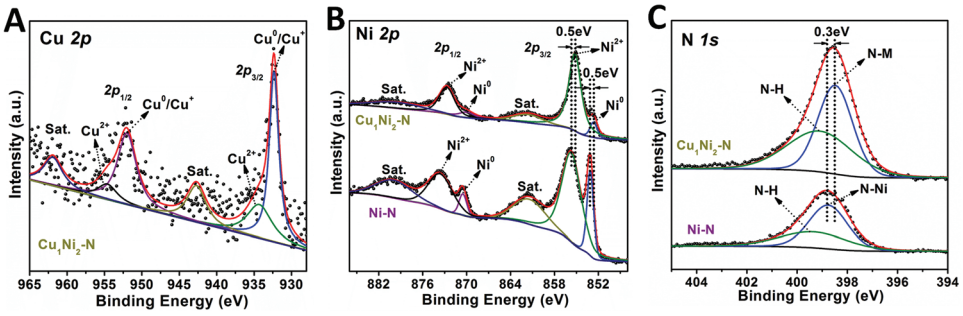

Figure 3. High-resolution XPS spectra. A) Cu 2p spectra of Cu_1Ni_2-N. B) Ni 2p and C) N 1s spectra of Cu_1Ni_2-N and Ni-N.

© 2019 WILEY-VCH Verlag GmbH & Co. KGaA, Weinheim

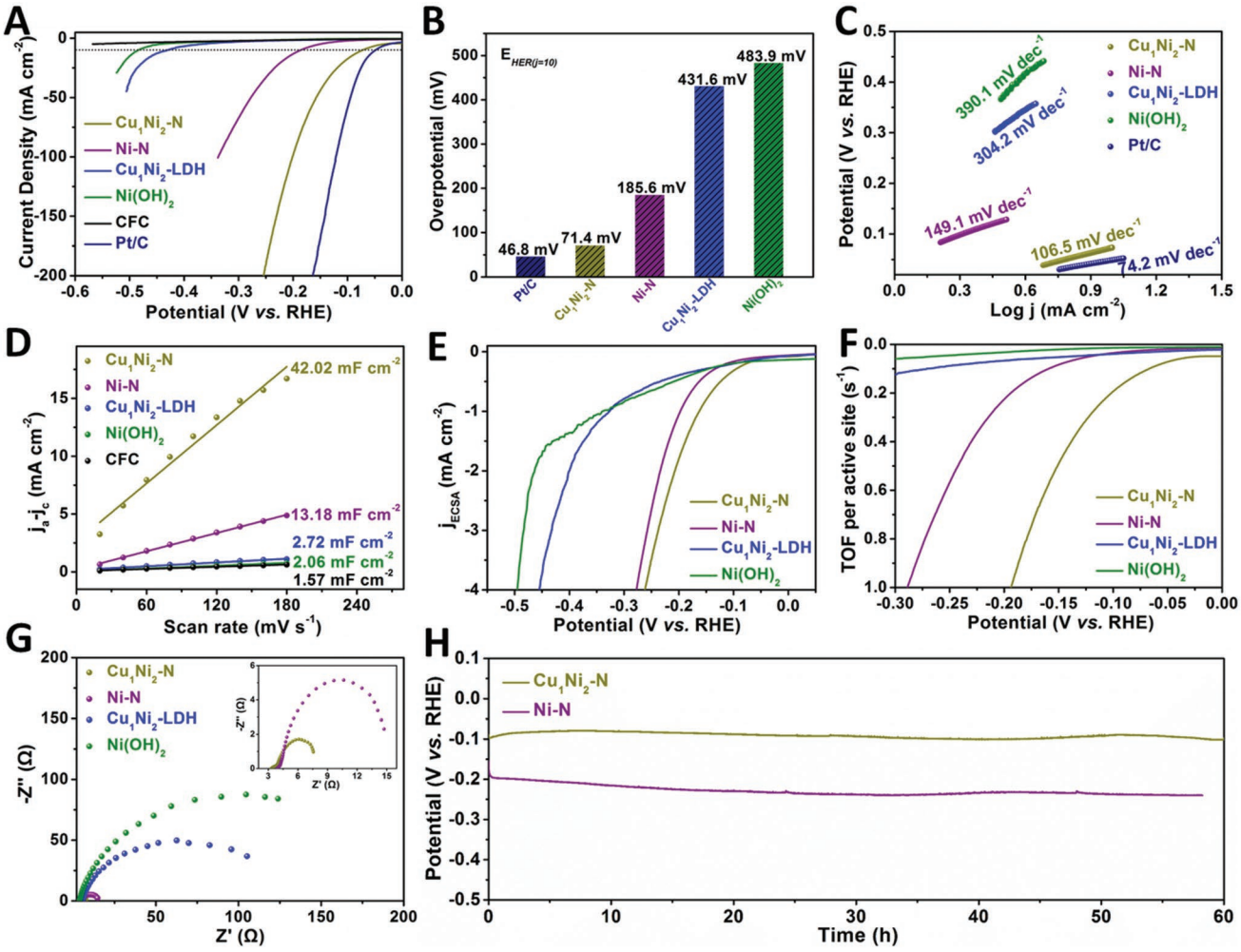

Figure 4. Electrocatalytic performance of electrodes for the HER measured in 1.0 M KOH solution. A) Polarization curves for Cu_1Ni_2-N, Ni-N, Cu_1Ni_2-LDH, $Ni(OH)_2$, Pt/C, and CFC at a scan rate of 5 mV s^{-1}. B) The overpotentials required for $j = 10$ mA cm^{-2} with different samples. C) The corresponding Tafel plots. D) Estimation of C_{dl} by plotting the current density at 0.124 V vs RHE. E) Polarization curves of different samples normalized by the electrochemical active surface area (ECSA). F) The turnover frequencies (TOFs) at different potentials. G) Electrochemical impedance spectroscopy for the corresponding electrocatalysts. H) Long-time stability test of the of Cu_1Ni_2-N and Ni-N at a constant current densities of 10 mA cm^{-2}.

in **Figure 4**A and Figure S12A, Supporting Information, the onset potential of Cu_1Ni_2-N electrode is much smaller at around 18 mV when compared with Ni-N (113 mV), Cu-N (214 mV), Cu_1Ni_2-LDH (367 mV), $Ni(OH)_2$ (443 mV), and Cu-pre (273 mV). Additionally, at a current density of 10 mA cm^{-2}, the Cu_1Ni_2-N electrode exhibits the lowest overpotential of 71.4 mV, compared with Ni-N (185.6 mV), Cu-N (317 mV), Cu_1Ni_2-LDH (431.6 mV), $Ni(OH)_2$ (483.9 mV), and Cu-pre (398 mV). The Cu_1Ni_2-N displays exceptional superior catalytic activity for HER over the other recently reported highly efficient noble metal-free catalysts, such as Ni-doped FeP (95 mV),[22] Ni_3FeN/r-GO (94 mV),[26] NC@ $CuCoN_x$ (105 mV),[27] $(Co_{1-x}Ni_x)(S_{1-y}P_y)_2$/G (117 mV),[77] NG-NiFe@MoC_2 (150 mV),[78] listed in Table S1, Supporting Information. In Figure S9, Supporting Information, the catalyst prepared at a calcination temperature of 400 °C and a Cu/Ni molar ratio of 1:2 presents a greater activity for HER. By fitting the LSV curves of the catalysts, the corresponding Tafel plots can be obtained to evaluate the HER kinetics. Figure 4C and Figure S12B, Supporting Information, show that the Tafel slope of Cu_1Ni_2-N is 106.5 mV dec^{-1}, which is substantially lower than Ni-N (149.1 mV dec^{-1}), Cu-N (151.9 mV dec^{-1}), Cu_1Ni_2-LDH (304.2 mV dec^{-1}), $Ni(OH)_2$ (390.1 mV dec^{-1}) and Cu-pre (167.2 mV dec^{-1}). This means that the Cu_1Ni_2-N electrode shows an enhanced HER kinetics. To further understand the intrinsic activity of different catalysts, the double layer capacitance (C_{dl}) is evaluated to measure the electrochemically active surface area (ECSA). As illustrated in Figure 4D and Figure S10, Supporting Information, derived from the cyclic voltammograms (CV) at different scan rates, the ECSA of Cu_1Ni_2-N, Ni-N, Cu-N, Cu_1Ni_2-LDH, $Ni(OH)_2$, Cu-pre, and CFC was calculated to be 42.02, 13.18, 14.01, 2.72, 2.06, 7.19, and 1.57 mF cm^{-2}, respectively. Meanwhile, the roughness factors (RFs) of the samples were calculated (Figure S10H, Supporting Information). In contrast, the Cu_1Ni_2-N electrode exhibits the highest active surface area and RF, which can be mainly attributed to the porous nanosheet structure and large surface area. The ECSA-normalized

© 2019 WILEY-VCH Verlag GmbH & Co. KGaA, Weinheim

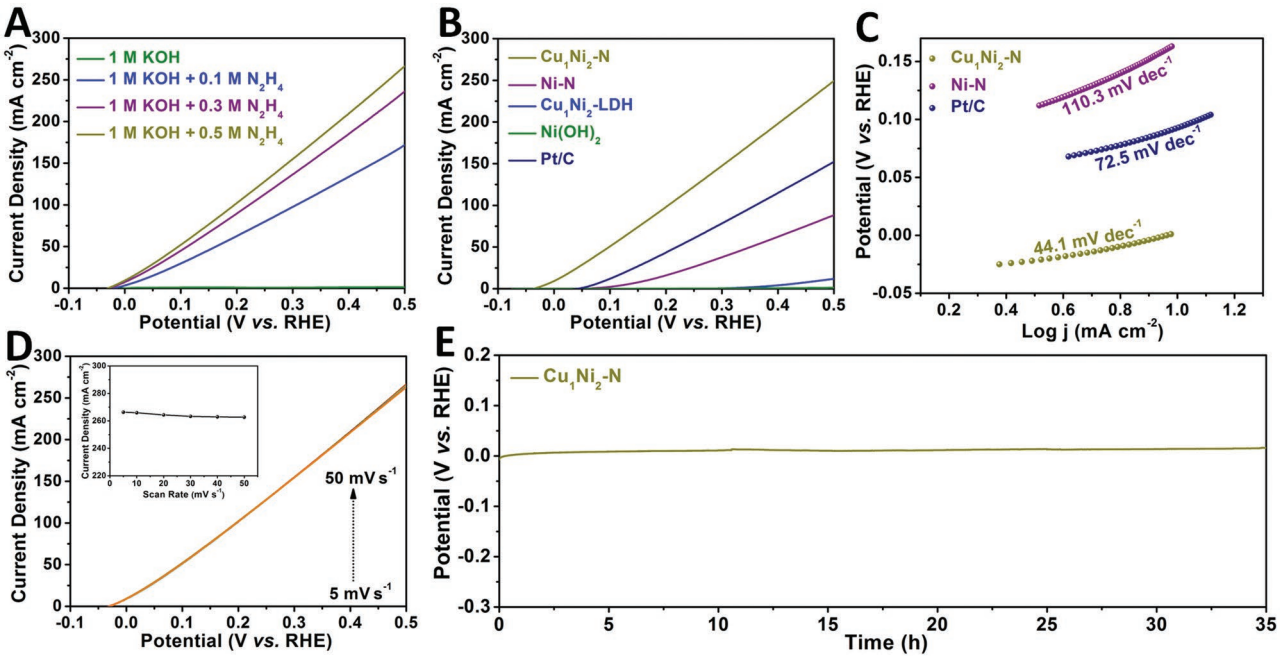

Figure 5. Electrocatalytic performance of electrodes for the HzOR. A) Polarization curves of Cu_1Ni_2-N toward different concentrations of hydrazine. B) Polarization curves of Cu_1Ni_2-N, Ni-N, Cu_1Ni_2-LDH, $Ni(OH)_2$, and Pt/C in 1.0 M KOH/0.5 M hydrazine electrolyte. C) The corresponding Tafel plots. D) Polarization curves of Cu_1Ni_2-N toward 0.5 M hydrazine at different scan rates (inset: the corresponding current density at 0.5 V for different scan rates). E) Long-time stability test of the of Cu_1Ni_2-N at a constant current density of 10 mA cm^{-2}.

LSV curves in Figure 4E and Figure S12D, Supporting Information, is utilized to highlight the intrinsic catalytic activity. It is obvious that the ECSA-normalized current density of Cu_1Ni_2-N is larger than that of Ni-N, Cu-N, Cu_1Ni_2-LDH, $Ni(OH)_2$, and Cu-pre at –0.2 V vs RHE, suggesting that the higher HER activity of Cu_1Ni_2-N results from not only the increased ECSA but also the enhanced intrinsic catalytic activity induced by the Cu_4N/Ni_3N interface. The turnover frequencies (TOFs) per surface site of catalysts were calculated to further evaluate intrinsic catalytic activities. The number of active sites was quantified from the CV plots tested in phosphate buffered solution.[19] Compared with nickel nitride, the bimetallic copper–nickel nitride provides more active sites (Figure S11, Supporting Information). The calculated TOF value of Cu_1Ni_2-N is 0.49 s^{-1} at the overpotential of 150 mV in Figure 4F, which is higher than those of Ni-N (0.08 s^{-1}), Cu-N (0.02 s^{-1}), Cu_1Ni_2-LDH (0.05 s^{-1}), $Ni(OH)_2$ (0.02 s^{-1}), and Cu-pre (0.01 s^{-1}). The tendency of TOF values is in full agreement with the intrinsic catalytic activity for HER, suggesting that the greatly enhanced HER activity of Cu_1Ni_2-N is mainly benefited from the synergistic catalytic effects induced by the intrinsic constructed interfaces between nickel nitride and copper nitride. Electrochemical impedance spectroscopy (EIS) measurements were conducted to investigate the electrode kinetics during the HER process. As shown in Figure 4G and Figure S12F, Supporting Information, the Nyquist plots indicate that the Cu_1Ni_2-N electrode possesses the smallest charge transfer resistance (R_{ct}) among all the samples, revealing a faster charge transfer and more favorable reaction kinetics for HER catalysis. Besides the catalytic activity, the durability of catalyst is also an important and challenging factor for practical applications. The long-term electrochemical stability at a current density of 10 mA cm^{-2} was tested by a chronoamperometry measurement with a negligible deactivation over 60 h (Figure 4H), confirming the excellent stability of Cu_1Ni_2-N toward HER.

We further investigated the OER performance of the Cu_1Ni_2-N electrode in 1 M KOH solution. It can deliver a current density of 20 mA cm^{-2} at low overpotential of 312 mV. For comparison, Ni-N, Cu-N, and IrO_2 require overpotential of 405, 498, and 324 mV to deliver the same current density, respectively (Figure S13, Supporting Information). Considering the undesirable overpotential of Cu_1Ni_2-N for OER (312 mV at 20 mA cm^{-2}), it will require much higher electrical energy to be utilized as the anode for water splitting. In contrast, HzOR provides an ideal anodic alternative due to its extremely low thermodynamic voltage of –0.33 V vs RHE.[53,55] Therefore, the cell voltage of water electrolysis can be greatly decreased by replacing the sluggish OER with the thermodynamically more favorable HzOR. We investigated the HzOR activities of samples in a three-electrode system at a scan rate of 5 mV s^{-1} in alkaline electrolyte. **Figure 5**A shows the LSV curves of Cu_1Ni_2-N electrode in 1.0 M KOH with different concentrations of hydrazine. It is obvious that no anodic current density is observed in the potential window of –0.1–0.5 V vs RHE when tested without hydrazine. In contrast, the addition of 0.1 M hydrazine solution results in a noticeable promotion in anodic current density. Meanwhile, the response current density rises along with the increasing concentration of hydrazine solution from 0.1 to 0.5 M. At high concentrations, such as 1 and 2 M hydrazine solution (Figure S16A, Supporting Information), the corresponding LSV curves are generally the same. Figure 5B and Figure S17, Supporting Information, present the

© 2019 WILEY-VCH Verlag GmbH & Co. KGaA, Weinheim

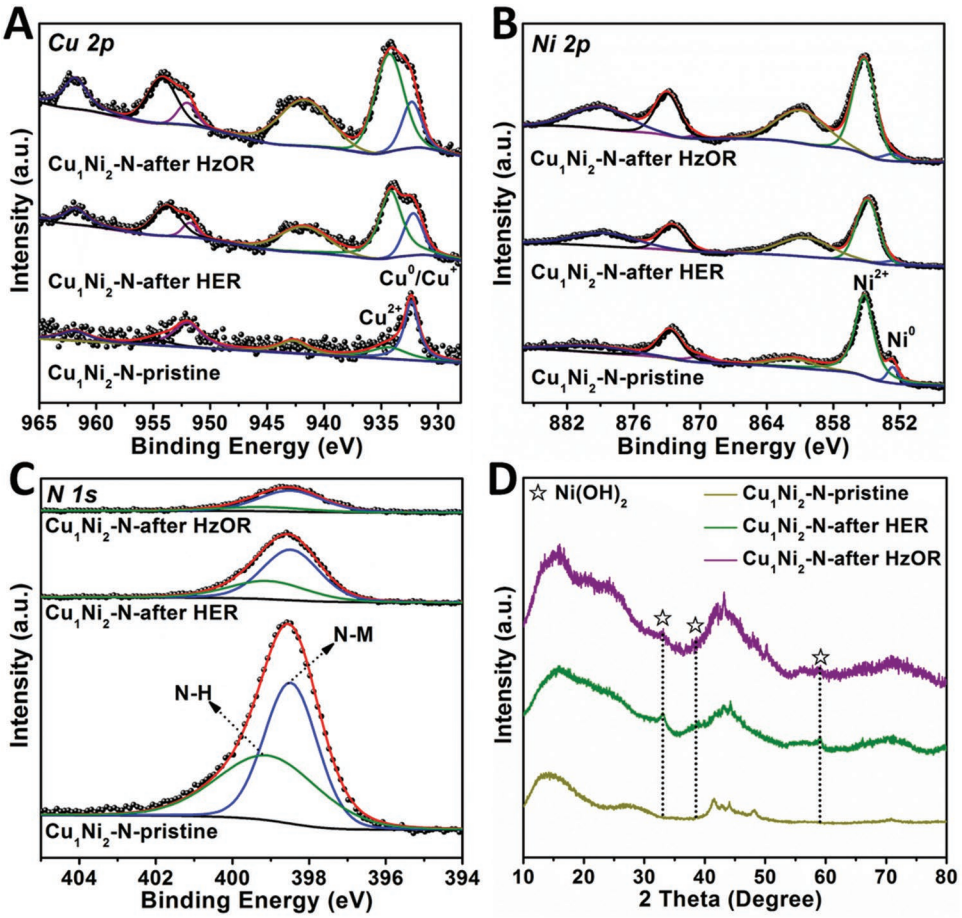

Figure 6. XPS and XRD characterization after HER and HzOR test. A) Cu 2p, B) Ni 2p, C) N 1s spectra, and D) XRD patterns of Cu_1Ni_2-N before and after HER and HzOR tests.

electrocatalytic HzOR activity of Cu_1Ni_2-N, Ni-N, Cu-N, Cu_1Ni_2-LDH, $Ni(OH)_2$, Cu-pre, and Pt/C electrodes measured in 1 M KOH/0.5 M hydrazine electrolyte. Both Cu_1Ni_2-LDH and $Ni(OH)_2$ samples display negligible anodic current density. The Cu_1Ni_2-N electrode possesses superior HzOR activity and can deliver anodic current density of 10 and 50 mA cm^{-2} at 0.5 and 96.9 mV, respectively, indicating a more negative value than those of Ni-N, Cu-N, and Pt/C electrodes. We also investigated the performance of electrodes with different Cu/Ni molar ratios (Figure S16B, Supporting Information). It is obvious that the catalyst with a Cu/Ni molar ratio of 1:2 exhibits the highest activity for HzOR. As displayed in Figure 5C and Figure S17B, Supporting Information, the Tafel slope of Cu_1Ni_2-N electrode (44.1 mV dec^{-1}) is much smaller than that of Ni-N (110.3 mV dec^{-1}), Cu-N (62.9 mV dec^{-1}), and Pt/C (72.5 mV dec^{-1}), which suggests that it has more favorable catalytic kinetics for HzOR. There are no apparent changes in the LSV curves at the different scan rates from 5 to 50 mV s^{-1}, revealing the efficient charge and mass transport in HzOR catalytic process.[47,63] As presented in Figure 5E, the Cu_1Ni_2-N electrode shows an outstanding long-term stability when tested at a constant current density of 10 mA cm^{-2} for 35 h with insignificant potential decay.

To get further insight of the catalytic reaction, the morphology and structural and chemical states of Cu_1Ni_2-N electrode were investigated after HER and HzOR. In Figure S19A–C, Supporting Information, the nanosheet morphology of the Cu_1Ni_2-N is retained well after long-term HER measurement as evidenced by SEM images. The porous structure and nanoparticles could be also viewed from TEM and HAADF-STEM images (Figure S19D,G, Supporting Information). In the HRTEM image (Figure S19E, Supporting Information), the lattice fringe spacings of 0.214 and 0.219 nm are well indexed to the (002) plane of Ni_3N and (111) plane of Cu_4N, respectively. This result confirms that the major nitride phases could be maintained during electrolysis. However, Figure S19F, Supporting Information, displays the lattice fringe spacings of 0.236 nm, which could be attributed to the (101) plane of $Ni(OH)_2$. The element mapping shows the distribution of Cu, Ni, N, and O in the nanosheet. Furthermore, three small diffraction peaks at 33.1°, 38.5°, and 59.2° could be assigned to the (100), (101), and (110) planes of $Ni(OH)_2$ in the XRD pattern after HER (**Figure 6**D). XPS analysis was further studied to verify the transformation on the surface of the catalyst after HER. In comparison with the XPS spectrum of original Cu_1Ni_2-N, the peak intensities of low-valent Cu (932.3 eV) and Ni (852.6 eV) decrease, while the peak intensities of high-valent Cu (935.1 eV) and Ni (855.2 eV) increase after HER measurement (Figure 6A,B).

© 2019 WILEY-VCH Verlag GmbH & Co. KGaA, Weinheim

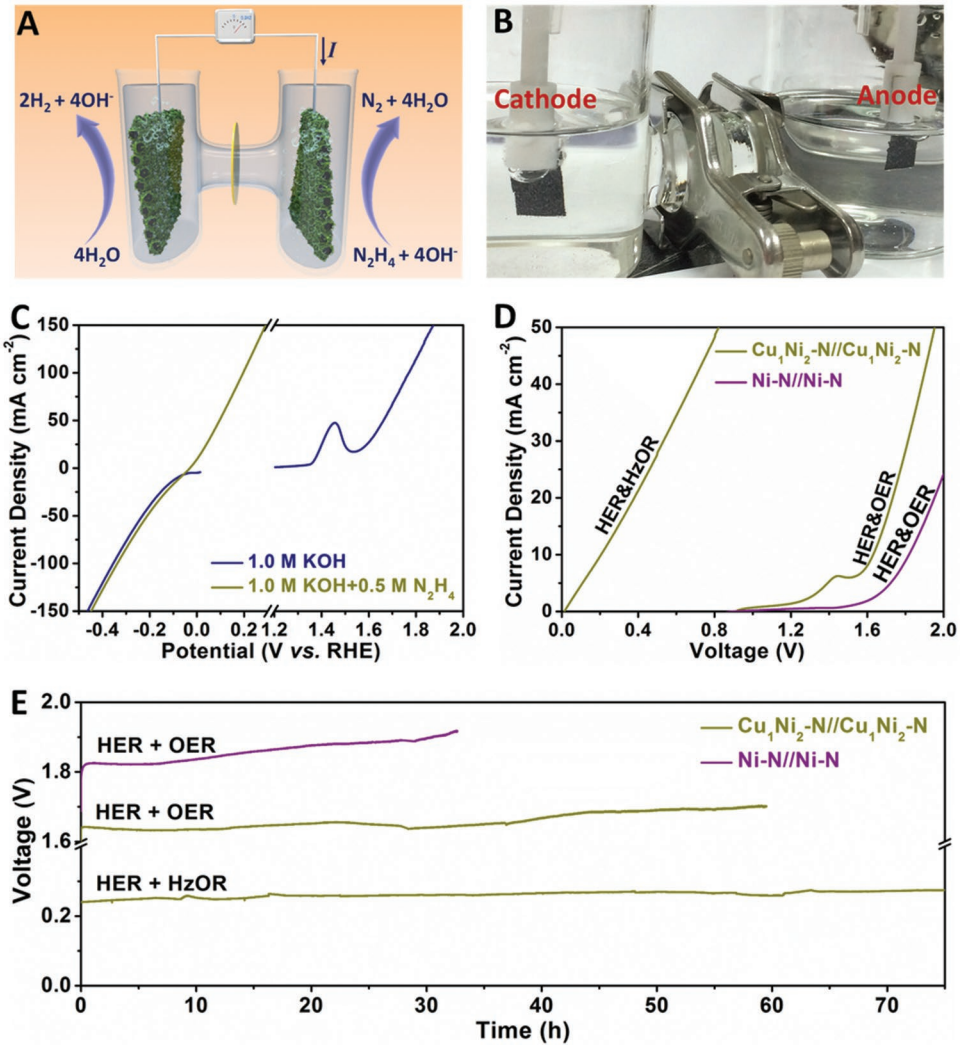

Figure 7. Performance of hydrazine-assisted water electrolysis for hydrogen production. A) The schematic illustration of two-electrode cell using Cu_1Ni_2-N electrode as both anode and cathode for hydrazine-assisted water electrolysis. B) Digital photograph of the two-electrode configuration. C) Polarization curves of Cu_1Ni_2-N for HER, OER, and HzOR without iR-corrected. D) Comparison of polarization curves for water electrolysis with and without hydrazine at a scan rate of 5 mV s^{-1}. E) Long-time stability tests of water electrolysis with and without hydrazine at a constant current density of 10 mA cm^{-2}.

Moreover, the N signal still could be detected in Figure 6C. These observations indicate that $Ni(OH)_2$ was generated on the surface of the Cu_1Ni_2-N after HER catalysis. Similar results could be also obtained after HzOR (Figure 6A,B; Figure S20, Supporting Information). This observation might be attributed to the thermodynamic instability of the nitride surface during the electrocatalytic reactions. This kind of hydroxylated phenomenon during electrolysis has also been reported in the previous works.[18,77,79] The hydroxide species produced from nitrides during electrolysis probably offer the favorable active sites for hydroxyl adsorption.[16,67,80] Meanwhile, the remaining nitrides provide the active sites for intermediates adsorption and support the efficient transport of electrons. Recently, the Ni-based hydroxides in the composite catalysts have been able to act as the water dissociation promoter and hydroxyl acceptor, which could favor the absorption of H_2O and optimize catalyst-intermediate energetics to accelerate the catalytic kinetics.[16,67] Besides, disordered structures and rich defects could be created during the process of electrolysis (Figures S19E,F and S20E,F, Supporting Information), which could promote the catalytic activity.[81,82]

As shown in Figure S16D, Supporting Information, the LSV curves of Cu_1Ni_2-N electrode for HER only presents a small positive shift of 13 mV in 1.0 M KOH/0.5 M hydrazine electrolyte, indicating that excellent HER activity can be retained with the presence of hydrazine. Inspired by the superior HzOR and HER catalytic performance of the Cu_1Ni_2-N electrode (**Figure 7**C), we assembled a two-electrode cell employing the Cu_1Ni_2-N electrode as both anode and cathode for water electrolysis as schematically presented in Figure 7A. Besides, the two-electrode system integrated with OER and HER was also measured in 1 M KOH electrolyte for comparison. Digital photograph of the two-electrode configuration toward hydrazine-assisted hydrogen generation during operation is shown

© 2019 WILEY-VCH Verlag GmbH & Co. KGaA, Weinheim

in Figure 7B. For water splitting, the two-electrode systems utilizing Cu_1Ni_2-N and Ni-N electrode require much larger voltage of 1.63 and 1.82 V, respectively, to reach the 10 mA cm^{-2} in 1 M KOH solution, while the hydrazine-assisted electrolysis system assembled with Cu_1Ni_2-N electrode delivers a cell voltage of only 0.24 V. Additionally, it presents a robust stability with a negligible deactivation over 75 h in Figure 7E. Comparing with the recently reported state-of-the-art bifunctional catalysts, Cu_1Ni_2-N electrode exhibits a superior activity for water electrolysis (Table S2, Supporting Information). Vigorous gas bubbles can be clearly observed on the individual electrode surfaces (Movie S2, Supporting Information). The amount of hydrogen generated from the cathode was collected by a drainage system during electrolysis. As shown in Figure S18, Supporting Information, the agreement of the amount of hydrogen gas determined by experimentally and theoretical suggests a Faradaic efficiency of nearly 95%.

Density functional theory (DFT) calculations were performed to gain insight into the outstanding catalytic activity of Cu_1Ni_2-N with Cu_4N/Ni_3N interface. Figure S21, Supporting Information, exhibits the schematic models, total and partial electronic density of states (DOS) for Cu_4N-Ni_3N, Cu_4N, and Ni_3N. It is clear that the three kinds of metal nitrides have no band gap in the band structure, which indicates the metallic nature. Meanwhile, electron occupied states near the Fermi level on Cu_4N-Ni_3N are much higher than those of Cu_4N and Ni_3N, revealing higher electrical conductivity and stronger carrier density. Notably, the d-band center of Cu_4N-Ni_3N (–2.24 eV) is downshifted from the Fermi level in comparison with Ni_3N (–1.61 eV), which might decrease the chemical adsorption capability. According to the previous studies,[13,83–86] the downward shift of d-band center basically lowers the energy of antibonding states below the Fermi level, leading to favorable adsorption of intermediates and thus high catalytic activity. On the basis of DFT calculations, it indicates that constructing Cu_4N/Ni_3N interface leads to a positive effect on the electronic characteristics compared with individual nitrides. Cu_1Ni_2-N with Cu_4N/Ni_3N interface possesses excellent electrical conductivity and fast charge transfer kinetic, which is beneficial to the catalytic reactions.

The superior catalytic activity of Cu_1Ni_2-N electrode could be ascribed to the following advantages. i) The porous nanosheet morphology assembled by nanoparticles provides large specific surface area with more catalytic active sites, simultaneously enhancing the transfer of electrolyte ion. ii) 3D catalyst electrode with highly open networks exhibits superhydrophilic behavior, facilitating the penetration of electrolyte and release of gas for electrolysis.[18] iii) As confirmed by experiments and DFT calculations, Cu_1Ni_2-N possesses good electric conductivity which is favorable for fast electron transport in the electrocatalytic reactions. iv) DOS reveals that the d-band center is downshifted from the Fermi level after Cu_4N incorporation, which decreases the binding strength of H. The strongly coupled interactions between Ni_3N and Cu_4N probably induces the redistribution of charge on the interfaces. This would adjust the electronic structure of materials surface and optimize the adsorption energy of reaction intermediates in the catalytic reactions, synergistically promoting the intrinsic activity.[15,49,75,87] v) The hydroxide species generated from nitrides after the catalytic reactions probably offer the favorable active sites for hydroxyl adsorption to accelerate the catalytic kinetics.[16,67] vi) Disordered structures and rich defects created during the electrolysis process could provide strong support for the high catalytic activity.[81,82] All these advantages greatly contribute to the high performance of Cu_1Ni_2-N electrode and enable it to be a promising alternative for energy-saving hydrogen production.

3. Conclusions

In summary, a class of copper–nickel-based nitride has been successfully constructed on the 3D substrate with rational design for efficient hydrogen generation in the alkaline electrolyte with hydrazine. Benefiting from the high electrical conductivity, porous morphology of interconnected nanostructures with large surface area, superhydrophilic electrode surface, synergistic catalytic effects of nickel nitride and copper nitride, hydroxide species, and disordered structures generated during the catalytic reactions, the prepared electrode presents exceptional catalytic performance and great stability for HER and HzOR, respectively. A two-electrode water electrolysis system assembled with the Cu_1Ni_2-N electrode as both cathode and anode delivers a small cell voltage of 0.24 V at a current density of 10 mA cm^{-2} over 75 h in 1 M KOH/0.5 M hydrazine electrolyte. This work provides new insights for designing and constructing the low-cost and high activity transition metal-based bifunctional catalytic electrode for energy-saving hydrogen production.

Supporting Information

Supporting Information is available from the Wiley Online Library or from the author.

Acknowledgements

This work was supported by the National Natural Science Fund for Distinguished Young Scholars (51425204), the National Natural Science Foundation of China (21673171, 51502226, 51802239), the National Key Research and Development Program of China (2016YFA0202603, 2018FYB0104202), the National Basic Research Program of China (2013CB934103), the Program of Introducing Talents of Discipline to Universities (B17034), the Fundamental Research Funds for the Central Universities (WUT: 2018IVA091). The authors are very grateful to Prof. Yan Zhao and Dr. Yalong Jiang for their generous assistance with the DFT calculations.

Conflict of Interest

The authors declare no conflict of interest.

Keywords

bifunctional catalysts, copper–nickel nitride, hydrazine oxidation, hydrogen evolution, water electrolysis

Received: January 31, 2019
Revised: March 28, 2019
Published online:

© 2019 WILEY-VCH Verlag GmbH & Co. KGaA, Weinheim

[1] J. A. Turner, *Science* **2004**, *305*, 972.
[2] S. Chu, Y. Cui, N. Liu, *Nat. Mater.* **2017**, *16*, 16.
[3] T. E. Mallouk, *Nat. Chem.* **2013**, *5*, 362.
[4] M. Dresselhaus, I. Thomas, *Nature* **2001**, *414*, 332.
[5] B. You, Y. Sun, *Acc. Chem. Res.* **2018**, *51*, 1571.
[6] I. Roger, M. A. Shipman, M. D. Symes, *Nat. Rev. Chem.* **2017**, *1*, 0003.
[7] Y. Shi, B. Zhang, *Chem. Soc. Rev.* **2016**, *45*, 1529.
[8] N. Cheng, S. Stambula, D. Wang, M. N. Banis, J. Liu, A. Riese, B. Xiao, R. Li, T.-K. Sham, L.-M. Liu, G. A. Botton, X. Sun, *Nat. Commun.* **2016**, *7*, 13638.
[9] C. C. McCrory, S. Jung, J. C. Peters, T. F. Jaramillo, *J. Am. Chem. Soc.* **2013**, *135*, 16977.
[10] Y. Lee, J. Suntivich, K. J. May, E. E. Perry, S.-H. Yang, *J. Phys. Chem. Lett.* **2012**, *3*, 399.
[11] Y. Shen, Y. Zhou, D. Wang, X. Wu, J. Li, J. Xi, *Adv. Energy Mater.* **2018**, *8*, 1701759.
[12] J. Zhang, T. Wang, P. Liu, Z. Liao, S. Liu, X. Zhuang, M. Chen, E. Zschech, X. Feng, *Nat. Commun.* **2017**, *8*, 15437.
[13] Y. Wu, X. Liu, D. Han, X. Song, L. Shi, Y. Song, S. Niu, Y. Xie, J. Cai, S. Wu, J. Kang, J. Zhou, Z. Chen, X. Zheng, X. Xiao, G. Wang, *Nat. Commun.* **2018**, *9*, 4531.
[14] J. Hou, B. Zhang, Z. Li, S. Cao, Y. Sun, Y. Wu, Z. Gao, L. Sun, *ACS Catal.* **2018**, *8*, 4612.
[15] J. Zhang, T. Wang, D. Pohl, B. Rellinghaus, R. Dong, S. Liu, X. Zhuang, X. Feng, *Angew. Chem.* **2016**, *128*, 6814.
[16] J. Hu, C. Zhang, L. Jiang, H. Lin, Y. An, D. Zhou, M. K. Leung, S. Yang, *Joule* **2017**, *1*, 383.
[17] L. Fang, W. Li, Y. Guan, Y. Feng, H. Zhang, S. Wang, Y. Wang, *Adv. Funct. Mater.* **2017**, *27*, 1701008.
[18] H. Liang, A. N. Gandi, D. H. Anjum, X. Wang, U. Schwingenschlögl, H. N. Alshareef, *Nano Lett.* **2016**, *16*, 7718.
[19] F. Yu, H. Zhou, Y. Huang, J. Sun, F. Qin, J. Bao, W. A. Goddard III, S. Chen, Z. Ren, *Nat. Commun.* **2018**, *9*, 2551.
[20] H. Zhang, X. Li, A. Hähnel, V. Naumann, C. Lin, S. Azimi, S. L. Schweizer, A. W. Maijenburg, R. B. Wehrspohn, *Adv. Funct. Mater.* **2018**, *28*, 1706847.
[21] J. Song, C. Zhu, B. Z. Xu, S. Fu, M. H. Engelhard, R. Ye, D. Du, S. P. Beckman, Y. Lin, *Adv. Energy Mater.* **2017**, *7*, 1601555.
[22] X. F. Lu, L. Yu, X. W. D. Lou, *Sci. Adv.* **2019**, *5*, eaav6009.
[23] J. Jia, T. Xiong, L. Zhao, F. Wang, H. Liu, R. Hu, J. Zhou, W. Zhou, S. Chen, *ACS Nano* **2017**, *11*, 12509.
[24] Y. Huang, J. Hu, H. Xu, W. Bian, J. Ge, D. Zang, D. Cheng, Y. Lv, C. Zhang, J. Gu, Y. Wei, *Adv. Energy Mater.* **2018**, *8*, 1800789.
[25] H. Yan, Y. Xie, Y. Jiao, A. Wu, C. Tian, X. Zhang, L. Wang, H. Fu, *Adv. Mater.* **2018**, *30*, 1704156.
[26] Y. Gu, S. Chen, J. Ren, Y. A. Jia, C. Chen, S. Komarneni, D. Yang, X. Yao, *ACS Nano* **2018**, *12*, 245.
[27] J. Zheng, X. Chen, X. Zhong, S. Li, T. Liu, G. Zhuang, X. Li, S. Deng, D. Mei, J. G. Wang, *Adv. Funct. Mater.* **2017**, *27*, 1704169.
[28] A. Wu, Y. Xie, H. Ma, C. Tian, Y. Gu, H. Yan, X. Zhang, G. Yang, H. Fu, *Nano Energy* **2018**, *44*, 353.
[29] J. Hou, Y. Sun, Z. Li, B. Zhang, S. Cao, Y. Wu, Z. Gao, L. Sun, *Adv. Funct. Mater.* **2018**, *28*, 1803278.
[30] H. Jin, X. Liu, A. Vasileff, Y. Jiao, Y. Zhao, Y. Zheng, S. Z. Qiao, *ACS Nano* **2018**, *12*, 12761.
[31] Y. Ma, Z. He, Z. Wu, B. Zhang, Y. Zhang, S. Ding, C. Xiao, *J. Mater. Chem. A* **2017**, *5*, 24850.
[32] Z. Li, W. Niu, L. Zhou, Y. Yang, *ACS Energy Lett.* **2018**, *3*, 892.
[33] P. Zhang, L. Li, D. Nordlund, H. Chen, L. Fan, B. Zhang, X. Sheng, Q. Daniel, L. Sun, *Nat. Commun.* **2018**, *9*, 381.
[34] L. Yu, H. Zhou, J. Sun, F. Qin, F. Yu, J. Bao, Y. Yu, S. Chen, Z. Ren, *Energy Environ. Sci.* **2017**, *10*, 1820.
[35] S. H. Ye, Z. X. Shi, J. X. Feng, Y. X. Tong, G. R. Li, *Angew. Chem., Int. Ed.* **2018**, *57*, 2672.
[36] H. Zhou, F. Yu, Q. Zhu, J. Sun, F. Qin, L. Yu, J. Bao, Y. Yu, S. Chen, Z. Ren, *Energy Environ. Sci.* **2018**, *11*, 2858.
[37] W. Li, X. Gao, D. Xiong, F. Wei, W. G. Song, J. Xu, L. Liu, *Adv. Energy Mater.* **2017**, *7*, 1602579.
[38] Z. Wang, J. Li, X. Tian, X. Wang, Y. Yu, K. A. Owusu, L. He, L. Mai, *ACS Appl. Mater. Interfaces* **2016**, *8*, 19386.
[39] J. Li, D. Fan, M. Wang, Z. Wang, Z. Liu, K. Zhao, L. Zhou, L. Mai, *ChemElectroChem* **2019**, *6*, 331.
[40] Y. Sun, K. Xu, Z. Wei, H. Li, T. Zhang, X. Li, W. Cai, J. Ma, H. J. Fan, Y. Li, *Adv. Mater.* **2018**, *30*, 1802121.
[41] C. Xia, Q. Jiang, C. Zhao, M. N. Hedhili, H. N. Alshareef, *Adv. Mater.* **2016**, *28*, 77.
[42] A. Grimaud, K. J. May, C. E. Carlton, Y.-L. Lee, M. Risch, W. T. Hong, J. Zhou, S.-H. Yang, *Nat. Commun.* **2013**, *4*, 2439.
[43] M. T. Koper, *J. Electroanal. Chem.* **2011**, *660*, 254.
[44] T. Take, K. Tsurutani, M. Umeda, *J. Power Sources* **2007**, *164*, 9.
[45] L. Dai, Q. Qin, X. Zhao, C. Xu, C. Hu, S. Mo, Y. O. Wang, S. Lin, Z. Tang, N. Zheng, *ACS Cent. Sci.* **2016**, *2*, 538.
[46] Z. Pu, I. S. Amiinu, F. Gao, Z. Xu, C. Zhang, W. Li, G. Li, S. Mu, *J. Power Sources* **2018**, *401*, 238.
[47] S. Chen, J. Duan, A. Vasileff, S. Z. Qiao, *Angew. Chem., Int. Ed.* **2016**, *55*, 3804.
[48] Z.-Y. Yu, C.-C. Lang, M.-R. Gao, Y. Chen, Q.-Q. Fu, Y. Duan, S.-H. Yu, *Energy Environ. Sci.* **2018**, *11*, 1890.
[49] C. Li, Y. Liu, Z. Zhuo, H. Ju, D. Li, Y. Guo, X. Wu, H. Li, T. Zhai, *Adv. Energy Mater.* **2018**, *8*, 1801775.
[50] J.-Y. Zhang, X. Tian, T. He, S. Zaman, M. Miao, Y. Yan, K. Qi, Z. Dong, H. Liu, B. Y. Xia, *J. Mater. Chem. A* **2018**, *6*, 15653.
[51] F. Li, J. Chen, D. Zhang, W.-F. Fu, Y. Chen, Z. Wen, X.-J. Lv, *Chem. Commun.* **2018**, *54*, 5181.
[52] B. You, N. Jiang, X. Liu, Y. Sun, *Angew. Chem.* **2016**, *128*, 10067.
[53] J. Y. Zhang, H. Wang, Y. Tian, Y. Yan, Q. Xue, T. He, H. Liu, C. Wang, Y. Chen, B. Y. Xia, *Angew. Chem. Int. Ed.* **2018**, *130*, 7775.
[54] J. Wang, X. Ma, T. Liu, D. Liu, S. Hao, G. Du, R. Kong, A. M. Asiri, X. Sun, *Mater. Today Energy* **2017**, *3*, 9.
[55] L. S. Wu, H. B. Dai, X. P. Wen, P. Wang, *ChemElectroChem* **2017**, *4*, 1944.
[56] Y. Hao, Y. Xu, W. Liu, X. Sun, *Mater. Horiz.* **2018**, *5*, 108.
[57] Q. Qin, H. Jang, P. Li, B. Yuan, X. Liu, J. Cho, *Adv. Energy Mater.* **2018**, 1803312.
[58] V. Rosca, M. T. Koper, *Electrochim. Acta* **2008**, *53*, 5199.
[59] Y. Liang, Y. Zhou, J. Ma, J. Zhao, Y. Chen, Y. Tang, T. Lu, *Appl. Catal., B* **2011**, *103*, 388.
[60] K. Asazawa, K. Yamada, H. Tanaka, M. Taniguchi, K. Oguro, *J. Power Sources* **2009**, *191*, 362.
[61] H. Wang, Y. Ma, R. Wang, J. Key, V. Linkov, S. Ji, *Chem. Commun.* **2015**, *51*, 3570.
[62] X. Ma, J. Wang, D. Liu, R. Kong, S. Hao, G. Du, A. M. Asiri, X. Sun, *New J. Chem.* **2017**, *41*, 4754.
[63] C. Tang, R. Zhang, W. Lu, Z. Wang, D. Liu, S. Hao, G. Du, A. M. Asiri, X. Sun, *Angew. Chem.* **2017**, *129*, 860.
[64] L. Zhang, D. Liu, S. Hao, L. Xie, F. Qu, G. Du, A. M. Asiri, X. Sun, *ChemistrySelect* **2017**, *2*, 3401.
[65] M. Liu, R. Zhang, L. Zhang, D. Liu, S. Hao, G. Du, A. M. Asiri, R. Kong, X. Sun, *Inorg. Chem. Front.* **2017**, *4*, 420.
[66] Q. Shao, P. Wang, X. Huang, *Adv. Funct. Mater.* **2018**, *29*, 1806419.
[67] B. Zhang, J. Liu, J. Wang, Y. Ruan, X. Ji, K. Xu, C. Chen, H. Wan, L. Miao, J. Jiang, *Nano Energy* **2017**, *37*, 74.
[68] P. Chen, Y. Tong, C. Wu, Y. Xie, *Acc. Chem. Res.* **2018**, *51*, 2857.
[69] X. Cui, P. Xiao, J. Wang, M. Zhou, W. Guo, Y. Yang, Y. He, Z. Wang, Y. Yang, Y. Zhang, Z. Lin, *Angew. Chem., Int. Ed.* **2017**, *56*, 4488.
[70] B. Qiu, L. Cai, Y. Wang, Z. Lin, Y. Zuo, M. Wang, Y. Chai, *Adv. Funct. Mater.* **2018**, *28*, 1706008.
[71] L. Cai, B. Qiu, Z. Lin, Y. Wang, S. Ma, M. Wang, Y. H. Tsang, Y. Chai, *J. Mater. Chem. A* **2018**, *6*, 21445.

© 2019 WILEY-VCH Verlag GmbH & Co. KGaA, Weinheim

[72] B. Qiu, L. Cai, Y. Wang, S. Ma, Y. H. Tsang, Y. Chai, *Mater. Today Energy* **2019**, *11*, 89.
[73] J. Balamurugan, C. Li, T. D. Thanh, O.-K. Park, N. H. Kim, J. H. Lee, *J. Mater. Chem. A* **2017**, *5*, 19760.
[74] A. D. Jagadale, G. Guan, X. Li, X. Du, X. Ma, X. Hao, A. Abudula, *J. Power Sources* **2016**, *306*, 526.
[75] T. Liu, A. Li, C. Wang, W. Zhou, S. Liu, L. Guo, *Adv. Mater.* **2018**, *30*, 1803590.
[76] Y. Hou, M. Qiu, G. Nam, M. G. Kim, T. Zhang, K. Liu, X. Zhuang, J. Cho, C. Yuan, X. Feng, *Nano Lett.* **2017**, *17*, 4202.
[77] H. J. Song, H. Yoon, B. Ju, G. H. Lee, D. W. Kim, *Adv. Energy Mater.* **2018**, *8*, 1802319.
[78] Q. Hu, X. Liu, B. Zhu, L. Fan, X. Chai, Q. Zhang, J. Liu, C. He, Z. Lin, *Nano Energy* **2018**, *50*, 212.
[79] X. Wang, W. Li, D. Xiong, D. Y. Petrovykh, L. Liu, *Adv. Funct. Mater.* **2016**, *26*, 4067.
[80] P. W. Menezes, C. Panda, S. Loos, F. Bunschei-Bruns, C. Walter, M. Schwarze, X. Deng, H. Dau, M. Driess, *Energy Environ. Sci.* **2018**, *11*, 1287.
[81] M. Kuang, P. Han, L. Huang, N. Cao, L. Qian, G. Zheng, *Adv. Funct. Mater.* **2018**, *28*, 1804886.
[82] Q. Li, Z. Xing, D. Wang, X. Sun, X. Yang, *ACS Catal.* **2016**, *6*, 2797.
[83] B. Hammer, J. K. Nørskov, *Nature* **1995**, *376*, 238.
[84] Y. Pan, K. Sun, Y. Lin, X. Cao, Y. Cheng, S. Liu, L. Zeng, W.-C. Cheong, D. Zhao, K. Wu, Z. Liu, Y. Liu, D. Wang, Q. Peng, C. Chen, Y. Li, *Nano Energy* **2019**, *56*, 411.
[85] J. Greeley, J. K. Nørskov, M. Mavrikakis, *Annu. Rev. Phys. Chem.* **2002**, *53*, 319.
[86] C. Meng, T. Ling, T. Y. Ma, H. Wang, Z. Hu, Y. Zhou, J. Mao, X. W. Du, M. Jaroniec, S. Z. Qiao, *Adv. Mater.* **2017**, *29*, 1604607.
[87] F. Song, W. Li, J. Yang, G. Han, P. Liao, Y. Sun, *Nat. Commun.* **2018**, *9*, 4531.

© 2019 WILEY-VCH Verlag GmbH & Co. KGaA, Weinheim